Thermoelectric properties of marcasite-type compounds MSb_2 (M = Ta, Nb): A combined experimental and computational study

Shamim Sk, Naoki Sato* and Takao Mori*

Research Center for Materials Nanoarchitectonics (MANA), National Institute for Materials Science (NIMS), 1-1 Namiki, Tsukuba, Ibaraki 305-0044, Japan

E-mail: SATO.Naoki@nims.go.jp and MORI.Takao@nims.go.jp
*Corresponding author

Abstract. Here, we investigate the thermoelectric properties of the marcasite-type compounds MSb_2 (M = Ta, Nb) in the temperature range of 310–730 K. These compounds were synthesized by a solid-state reaction followed by the spark plasma sintering process. The Rietveld refinement method confirms the monoclinic phase with space group $C2/m$ for both compounds. The observed values of Seebeck coefficients exhibit non-monotonic behaviour in the studied temperature range, with the maximum magnitude of -14.4 and -22.7 μV K^{-1} for $TaSb_2$ and $NbSb_2$, respectively at ∼444 K. The negative sign of S in the full temperature window signifies the n-type behaviour of these compounds. Both electrical and thermal conductivities show decreasing trends with increasing temperature. The experimentally observed thermoelectric properties are understood through the first-principles DFT and Boltzmann transport equation. A pseudogap in the density of states around the Fermi level characterizes the semimetallic behaviour of these compounds. The multi-band electron and hole pockets were found to be mainly responsible for the temperature dependence of transport properties. The experimental power factors are found to be ∼0.09 and ∼0.42 mW m^{-1} K^{-2} at 300 K for $TaSb_2$ and $NbSb_2$, respectively. We found that there is much room for improvement of power factor by tuning carrier concentration. The DFT-based calculations predict the maximum possible power factors at fairly high doping concentrations. The present study suggests that the combined DFT and Boltzmann transport theory are found to be reasonably good at explaining the experimental transport properties, and moderate power factors are predicted.

Keywords: Thermoelectric properties, density functional theory, electronic structure, electron and hole pockets, semi-classical Boltzmann theory, power factor.

1. Introduction

The performance of thermoelectric (TE) materials is evaluated by the dimensionless figure-of-merit, $ZT = \frac{S^2\sigma T}{\kappa}$, where S is the Seebeck coefficient, σ is the electrical conductivity, κ is the thermal conductivity (which is the sum of electronic, κ_e and lattice thermal conductivity, κ_l), and T is the absolute temperature. The value of ZT determines the conversion efficiency; the higher the ZT value, the better the TE performance. Finding materials having ZT higher than unity is still a challenging task, though the research in TE has made in progress for many decades [1–7]. Actually, efficient TE materials have to pass through a typical tradeoff, which includes materials that are good electrical conductors but have poor thermal conductivity. This implies that the transport of charge carriers within the material should experience weak electron scattering and strong phonon scattering.

Realizing high ZT has always been a challenging task due to the strong correlation among the TE parameters through charge carriers [8, 9]. Till now, the state-of-the-art TE materials are Bi_2Te_3 [10, 11], Sb_2Te_3 [12]; PbTe [13, 14], SnTe [15]; and SiGe [16, 17] based compounds. Recently, the antimonides have gained increased interest with high performance discovered in Mg_3Sb_2-type materials for example [18–21]. The expression of ZT implies that there are two ways for boosting the TE performance: either by decreasing the lattice thermal conductivity without affecting or less affecting the electronic properties [1, 22–24] or by improving the power factor ($S^2\sigma$) [25–30].

In recent decades, the TE properties of $FeSb_2$ were extensively studied because of ultra-high S of up to -45000 µV K^{-1} at 12 K, resulting in the highest power factor reported ever [31, 32]. But, due to the large κ of $FeSb_2$, the ZT is diminished with the low value of 0.005 at 12 K [31, 32]. The $FeSb_2$ is a narrow-gap semiconductor with an orthorhombic marcasite structure [31, 32]. The TE properties of other marcasite-type compounds including XTe_2 (X = Fe, Co, Ni) [33], FeX_2 (X = Se, Te) [34], FeS_2 [35], $FeAs_2$ [36], $RuSb_2$ [36, 37], etc, have been studied in the last decades. Within the same family of marcasite-type compounds, the MSb_2 (M = Ta, Nb) with a monoclinic crystal structure (Space group: $C2/m$, No. 12) has recently attracted remarkable attention as Weyl semimetals exhibiting unusual magneto-transport properties [38–42]. As semimetals, these materials typically feature a small overlap of energy bands and the absence of a band gap, which can lead to a high power factor. However, their TE properties remain largely unexplored, particularly at elevated temperatures. For instance, Masuda *et al.* have studied the TE properties of $TaSb_2$ compound in the temperature range of 300–800 K [43]. They synthesized $TaSb_2$ using solid-state reaction method with the spark plasma-sintering process and explored the temperature dependent S and σ [43]. The experimental measurements of S and σ of MSb_2 (M = Ta, Nb) have been done by Failamani *et al.* [44] in the temperature range of 300–800 K. MSb_2 (M = Ta, Nb) are prominent compensated semimetals that exhibit resistivity plateaus under magnetic fields and anisotropic quasi-parabolic magnetoresistance at low temperatures [38, 45–49]. $TaSb_2$, in particular, shows negative longitudinal magnetoresistance and a nontrivial Berry phase at low temperatures [38, 47]. Additionally, $TaSb_2$ and $NbSb_2$ are distinctive as weak topological insulators in the absence of a magnetic field and can be categorized as type II Weyl materials when magnetic fields are applied [46,48]. Although the physics of MSb_2 (M = Ta, Nb) has been extensively studied, there is still a lack of theoretical understanding of the experimental TE properties of MSb2 (M = Ta, Nb) at elevated temperatures. In the present study, the TE properties of MSb_2 (M = Ta, Nb) are investigated using both experimental and computational tools at the high temperatures. The experimental TE properties of said compounds are understood using density functional theory (DFT)-based calculations, and we predict the possible maximum power factors with a suitable amount of doping.

In this work, we have synthesized marcasite-type compounds MSb_2 (M = Ta, Nb) using the combined solid-state reaction and spark plasma sintering process. All the TE properties are measured and analyzed. First-principle calculations and Boltzmann transport equations are utilized to understand the experimental results. The multi-band electron and hole pockets are found to reasonably explain the experimental data. The maximum possible power factors for p-type and n-type of MSb_2 (M = Ta, Nb) are also predicted using the DFT-based calculations.

2. Experimental and computational details

2.1. Synthesis

MSb_2 (M = Ta, Nb) were synthesized using a combined solid state reaction (SSR) and spark plasma sintering (SPS) process. The high purity powder of Ta (99.99%), Nb (99.99%) and Sb (99.99%) from Sigma-Aldrich were taken as starting materials. The desired amount of metal powder were ground in alumina mortar and cold pressed at 25 MPa to form pellets. Then the obtained pellets were heated at 700 °C for 3 days in vacuum-sealed quartz tube. Although the target phase for both compounds were obtained in SSR, but the pellets were too brittle for the transport measurements. In order to get dense pellets, we ground the SSR pellets and did the SPS (SPS-1080, SPS Syntex Inc.) at 750 °C for 8 minutes. During the SPS, the constant uniaxial pressure of 50 MPa was applied to a graphite punch of 10 mm diameter under a partial argon atmosphere. The relative densities were calculated from the sample densities determined by Archimedes principle, which are found to be ∼95% and ∼94% for $TaSb_2$ and $NbSb_2$, respectively. The obtained pellets were cut into the required dimensions for the transport measurements.

2.2. Characterization

X-ray diffraction (XRD) were taken (Smart Lab3, Rigaku) in 10–90° as shown in Fig. 1(a) and (b) for $TaSb_2$ and $NbSb_2$, respectively. Rietveld refinement method confirms the monoclinic phase with space group $C2/m$ (No. 12) for both compounds. The refined lattice parameters and angles are shown in Table I. The impurity peak at 28.7° (Fig. 1(a)) may arise from the surface oxide layer of Sb_2O_3 [43].

2.3. Thermoelectric measurement

The simultaneous measurement of the electrical conductivity and Seebeck coefficient were performed using ZEM-2 (ADVANCE RIKO) under partial helium environment. The dimensions of $TaSb_2$ and $NbSb_2$ were taken as $4.11 \times 1.92 \times 7.57$ mm^3 and $4.11 \times 1.62 \times 7.39$ mm^3, respectively. The thermal conductivity was obtained using the formula: $\kappa = D \times C_p \times \rho$. The ρ is the density of the sample. The D is the thermal diffusivity, which is measured using the laser flash diffusivity method implemented in LFA-467 Hyper flash (Netzsch) instrument. The heat capacity, C_p was estimated using a standard sample (pyroceram-9060) in LFA-467. The circular pellets of $TaSb_2$ and $NbSb_2$ with diameter of 10 mm and thickness of 1.3 mm and 1.6 mm, respectively were used for the measurements.

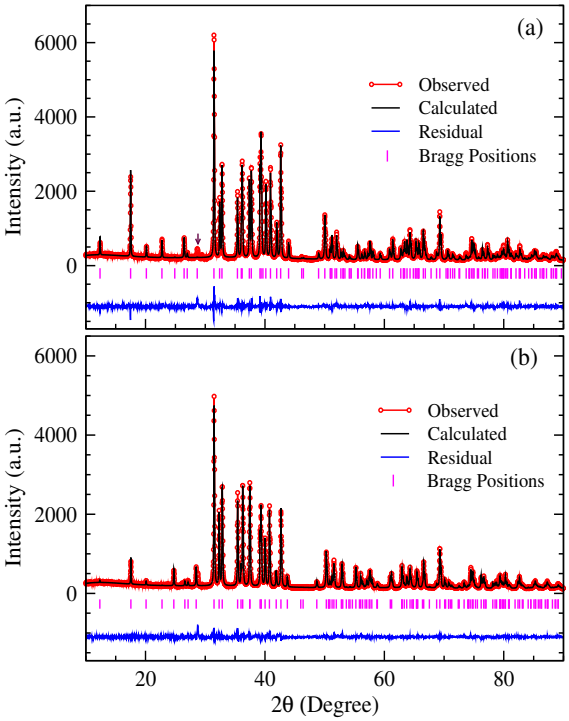

Figure 1: Measured room temperature X-ray diffraction patterns and calculated ones by Rietveld method of (a) $TaSb_2$ and (b) $NbSb_2$. The peak at 28.7° indicated by an arrow in (a) is an impurity peak.

Table 1: The experimental (obtained from the Rietveld refinement) and calculated (obtained from DFT) lattice parameters and angles of $TaSb_2$ and $NbSb_2$. The units of lattice parameters and angles are in Å and in degree, respectively. Parentheses refer to the estimated standard deviations.

	$TaSb_2$		$NbSb_2$	
	Exp.	Cal.	Exp.	Cal.
a	10.22203(9)	10.14321	10.23722(1)	10.16523
b	3.64461(9)	3.62423	3.63139(1)	3.59164
c	8.29068(4)	8.22734	8.33121(8)	8.25354
β	120.396(0)	120.534	120.026(4)	120.013

2.4. Computational details

The ground state electronic structure calculations are carried out within DFT [51]. The projector augmented-wave method is used as implemented in Quantum Espresso code [52]. The PERDEW-ZUNGER (LDA) [53] exchange-correlation (XC) functional is used for the calculation. The calculations are done in relaxed structure. The optimized lattice parameters and angles are tabulated in Table I. The force convergence criteria for structure relaxation was set to be 10^{-4} Ry/Bohr. Table II shows the relaxed atomic positions along with the experimental values for both compounds. The structures relaxed using DFT are closely matched with the experimental ones.

Table 2: Fractional coordinates of atomic positions for relaxed structure of $TaSb_2$ and $NbSb_2$. The experimental values are also mentioned in the parentheses.

$TaSb_2$	x (exp)	y (exp)	z (exp)	$NbSb_2$	x (exp)	y (exp)	z (exp)
Ta	0.150 (0.152)	0 (0)	0.188 (0.193)	Nb	0.151 (0.152)	0 (0)	0.190 (0.194)
Sb1	0.148 (0.143)	0 (0)	0.535 (0.532)	Sb1	0.149 (0.145)	0 (0)	0.536 (0.531)
Sb2	0.405 (0.401)	0 (0)	0.114 (0.111)	Sb2	0.405 (0.402)	0 (0)	0.115 (0.111)

The kinetic energy cut-off for wavefunctions is used as 60 Ry. The kinetic energy cut-off for charge density is set to be 8 times the kinetic energy cut-off for wavefunctions. The k-mesh grid was used as $7\times15\times7$ for both compounds. The energy convergence criteria was set to be 10^{-8} Ry for the self-consistent field calculation. The transport coefficients were calculated using the BoltzTraP2 package [54] interfaced with Quantum Espresso code [52]. For the transport properties calculations, the electronic structures are calculated applying the k-mesh of 30 × 60 × 30. The phonon dispersion is computed using density functional perturbation theory (DFPT), implemented in Quantum Espresso code. The q-mesh size of $2\times4\times2$ is used for force calculation. The convergence criteria for the calculations of forces is set as 10^{-14} Ry/Bohr.

3. Results and discussion

3.1. Experimental transport properties

Fig. 2(a) exhibits the experimentally measured Seebeck coefficients (S) of MSb_2 (M = Ta, Nb) in the temperature range of 310–730 K. The $|S|$ for both compounds are found to increase up to ∼450 K, then decreases till the highest temperature. The highest magnitudes of S are found to be −14.4 and −22.7 µV K^{-1} for $TaSb_2$ and $NbSb_2$, respectively at ∼444 K. Our experimental results align closely with the reported data [43, 44]. For instance, Masuda *et al.* reported the S of $TaSb_2$ as −12 µV K^{-1} at 500 K [43]. Similarly, Failamani *et al.* reported the S of $TaSb_2$ and $NbSb_2$ as −14 and −21 µV K^{-1}, respectively, at 500 K [44]. The total S mainly comes from the contributions of electrons and holes. Under the two-carrier conduction model, the S can be expressed as $S = \frac{S_h\sigma_h+S_e\sigma_e}{\sigma_h+\sigma_e}$ [55], where $S_{h,e}$ is the Seebeck coefficients of holes and electrons and $\sigma_{h,e}$ is the electrical conductivity of holes and electrons. The sign of the S is determined by the major contribution coming from the electrons or holes, because electrons generally yield the negative S, while holes give positive S. Therefore, the negative sign of S in Fig. 2(a) signifies the dominating n-type behaviour of these compounds. The magnitude of S for $NbSb_2$ is larger than that of $TaSb_2$ in the full temperature window. The temperature dependence of S shows a peak at around 444 K for both compounds, which suggests a compensation of p- and n-type charge carriers [50]. The non-linear behaviour of S with temperature for both compounds can be explained by the calculated band-structure, which is discussed later.

Fig. 2(b) shows the temperature dependence of electrical conductivities (σ) of $TaSb_2$ and $NbSb_2$. The σ are found to be 0.88 $\times10^6$ and 0.95 $\times10^6$ Ω^{-1} m^{-1} for $TaSb_2$ and $NbSb_2$, respectively at ∼310 K. Then as the temperature increases, the σ decreases till the highest temperature (∼730 K) with the corresponding values of 0.39 $\times10^6$ and 0.41 $\times10^6$ Ω^{-1} m^{-1} for $TaSb_2$ and $NbSb_2$, respectively. Our measured values of σ are accordance with the other experimentally reported data [43, 44]. For example, Masuda *et al.* reported the σ of 1.0 $\times10^6$ Ω^{-1} m^{-1} for $TaSb_2$ at 300 K [43], while Failamani *et al.* reported values of 1.11 $\times10^6$ Ω^{-1} m^{-1} and 1.18 $\times10^6$ Ω^{-1} m^{-1} for $TaSb_2$ and $NbSb_2$, respectively, at room temperature [44]. The decrement behaviour of σ can be explained by the simple formula: $\sigma = \frac{ne^2\tau}{m^*}$, where, n, e, τ and m^* are the carrier concentration, the electronic charge, the relaxation time and the effective mass of charge carriers, respectively. Generally, under the increment of temperature, n increases, whereas τ decreases. Hence, among the opposite trend of n and τ with temperature, the dominating behaviour generally gives the temperature dependent trend of σ. Hence, Fig. 2(b) shows that the temperature dependent τ is dominating over n in σ. In general, with increase in temperature, the σ of semiconductors increases, while σ of metals decreases. Hence, the temperature dependent trend of σ of present compounds show the metal-like behaviour. However, the electronic structure calculations predict the semimetallic (in between semiconductor and metals) behaviour of these compounds, which is discussed later.

Using the measured S and σ, the power factors are calculated as shown in Fig. 2(c). The calculated values of power factors are found to be ∼0.09 and ∼0.42 mW m^{-1} K^{-2} at 300 K for $TaSb_2$ and $NbSb_2$, respectively. At 750 K, the power factors are calculated as ∼0.03 and ∼0.08 mW m^{-1} K^{-2}, respectively. The comparable power factors of other marcasite-type compounds, including for $CoTe_2$ as 0.33 mW m^{-1} K^{-2} at 570 K [33], $FeSe_2$ as 0.12 mW m^{-1} K^{-2} at 554 K [56]

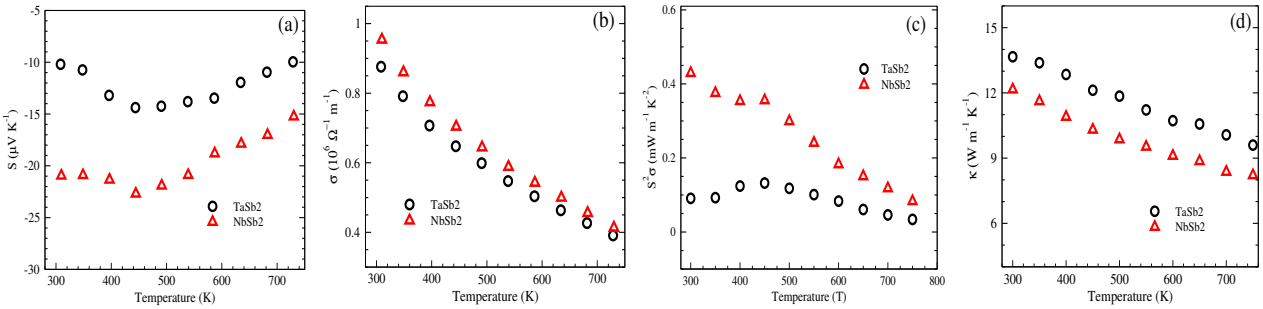

Figure 2: Temperature dependence of measured (a) Seebeck coefficient, S (b) electrical conductivity, σ (c) power factor, $S^2\ \sigma$ and (d) thermal conductivity, κ of $TaSb_2$ and $NbSb_2$.

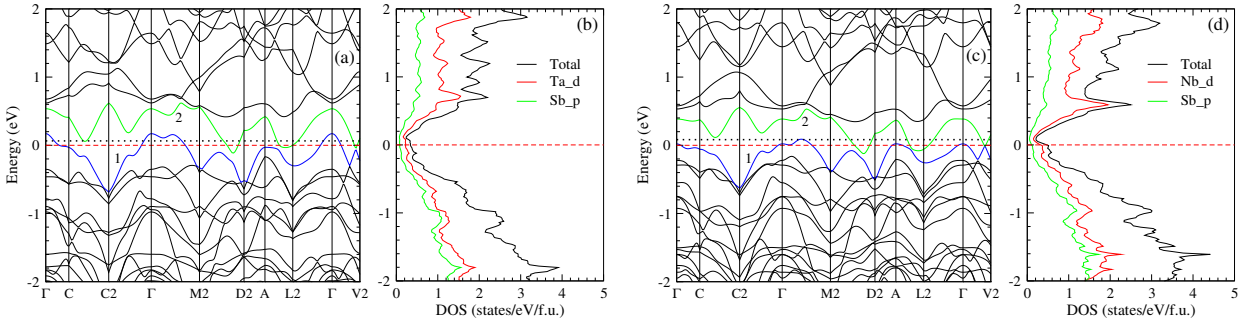

Figure 3: (a) Band-structure and (b) density of states (DOS) of $TaSb_2$; (c) band-structure and (d) DOS of $NbSb_2$. The coordinates of the high symmetry k-points are: Γ (0 0 0), C (0.27 0.29 0), C_2 (-0.29 0.7 0), M_2 (-0.5 0.5 0.5), D_2 (0.26 0.26 0.5), A (0 0 0.5), L_2 (0 0.5 0.5) and V_2 (0 0.5 0).

have been reported. Usually, semimetals possess low S with high σ. But recent studies have shown that the S of the semimetals can be tuned by magnetic field, strain, etc [57–59]. Semimetals having asymmetry in their electron and hole pockets could have high S [60, 61]. Semimetals with high (or fractionally low) electron (m_e^*) and hole (m_h^*) effective mass ratio results in high S [60, 62]. If the m_e^*/m_h^* ratio tends to 1, it signifies a very low magnitude of the S. For instance, HgTe possesses a high m_e^*/m_h^* ratio of $\approx$ 0.1, which results in high negative S between -90 and -135 μV K^{-1} at room temperature [60]. In our study, the m_e^*/m_h^* ratio for $TaSb_2$ is calculated as ∼1.2 (near to 1), which results in low magnitude of S.

The thermal conductivities (κ) of $TaSb_2$ and $NbSb_2$ are measured in the temperature region 300–750 K as shown in Fig. 2(d). The κ are gradually decreasing with the increment of temperature in the whole temperature range. At 300 K, the κ are found to be 13.7 and 12.2 W m^{-1} K^{-1}, while these are decreased to 9.6 and 8.2 W m^{-1} K^{-1} at 750 K for $TaSb_2$ and $NbSb_2$, respectively. In the full temperature window, the values of κ for $TaSb_2$ are higher than the $NbSb_2$. The total κ is a simple addition of electronic thermal conductivity (κ_e) and lattice thermal conductivity (κ_L), *i.e.*, $\kappa = \kappa_e + \kappa_L$. In this work, we have calculated the temperature dependence of κ_e for both compounds. The experimental κ_e can be estimated using the experimental σ via Wiedemann-Franz law: $\kappa_e = L\sigma T$, L is Lorenz number. Then it will be interesting to see how calculated κ_e explains the experimental κ_e, which is described later. As can be seen from the Fig. 2(b), the σ of $NbSb_2$ are higher than that of $TaSb_2$. Hence, larger values of κ_e are expected for $NbSb_2$ as compared to $TaSb_2$ according to the Wiedemann-Franz law.

3.2. Electronic structure

To understand the experimentally measured transport coefficients, we have calculated the electronic structure of MSb_2 (M = Ta, Nb). The band-structures for $TaSb_2$ and $NbSb_2$ are calculated along the lines between high symmetry points (Γ–C–C2–Γ–M2–D2–A–L2–Γ–V2) in the first Brillouin zone, which are shown in Fig. 3(a) and (c), respectively. The dashed red line corresponding to zero energy defines the Fermi level, E_F of the compounds. It is clear that the two bands (which are indexed by 1 and 2) around the E_F are expected to contribute to the transport properties of these compounds. In both Fig. 3(a) and (c), the occupied band 1 crosses the E_F at either side of the Γ point and becomes unoccupied, while the unoccupied band 2 crosses the E_F in the M2–D2, A–L2 and

Γ–V2 directions and becomes occupied. This type of mixing of occupied and unoccupied bands around the E_F predicts the semimetal-like character of the compound, which is consistent with the other reported works [38, 39, 41, 63]. The electronic band-structure is the key input for calculating any electronic transport properties. In the present study, we have calculated the Seebeck coefficient, electrical conductivity and electronic part of thermal conductivity for MSb_2 (M = Ta, Nb). We will recall this part in the next subsection during the discussion of calculated transport properties. We have also investigated the effect of spin-orbit coupling (SOC) on band structures and transport properties, and found that the effects were minor. All the results including SOC effects can be found in Supplemental Material (SM).

Fig. 3(b) and (d) express the calculated total and partial density of states (DOS) of $TaSb_2$ and $NbSb_2$, respectively. At E_F, the values of DOS are calculated as ∼0.34 and ∼0.47 states/eV/f.u. for $TaSb_2$ and $NbSb_2$, respectively. A pseudogap around the E_F characterizes the semimetallic behaviour of these compounds. In order to know the contributions in transport properties from different atoms, we have calculated the partial DOS of Ta, Nb and Sb as shown in the same figures. In the occupied band region, the contribution in the DOS comes from Ta(Nb)-d and Sb-p orbitals almost equally. In contrast, in the unoccupied band region, the dominant contribution in the DOS comes from Ta(Nb)-d orbitals, with the small contribution from Sb-p orbitals. In the energy range of −1 to 0 eV in the occupied band region of Fig. 3(b), the contributions of Ta-d and Sb-p in the DOS are calculated as ∼60% and ∼40%, while these contributions are found to be ∼80% and ∼20%, respectively, in the energy range of 0 to 1 eV in the unoccupied band region.

The effective mass (m^*) of electrons (m_e^*) and holes (m_h^*) are calculated using the formula: $m^* = \hbar^2/(d^2E/dk^2)$ under parabolic approximation [8]. Table III lists the m^* of bands 1 and 2 corresponding to different electron and hole pockets near the E_F in terms of electron's mass (m_e) of $TaSb_2$. These bands are named as B1 and B2 in the table. The effective mass ratio of m_e^*/m_h^* is calculated as ∼1.2, results in small magnitude of S.

The bulk modulus of $TaSb_2$ and $NbSb_2$ are also calculated. This is an elastic property of a material, which can be defined as: $B = -V\frac{(P-P1)}{(V-V1)}$, where V is the equilibrium volume, and P is the corresponding pressure. The $V1$ is the expanded/shrunk volume, and $P1$ is the corresponding pressure. The three calculations are performed, including the equilibrium lattice constant, +1% (expanded volume) and −1% (shrunk volume). The final B is calculated by taking the average of expanded and shrunk one, which are found to be ∼131 GPa and ∼125 GPa for $TaSb_2$ and $NbSb_2$, respectively. In Materials Project, the B are reported as 103 GPa and 98 GPa for $TaSb_2$ (mp - 11697 [64]) and $NbSb_2$ (mp - 1969 [65]), respectively. However, the B of $TaSb_2$ has been reported as 131.2 ± 3.4 by Zhou *et al.* [66], which gives close match with our calculation.

Table 3: Effective mass (m^*) of electrons (m_e^*) and holes (m_h^*) corresponding to bands 1 and 2 of $TaSb_2$.

Bands	Directions	m_e^*
B1	Γ–M2	5.45
B2	C–C2	1.69
B2	M2–D2	1.37
B2	A–L2	6.49
Bands	**Directions**	m_h^*
B1	Γ (C2–Γ–M2)	4.14
B1	Γ–M2	5.26
B1	Γ (L2–Γ–V2)	2.26

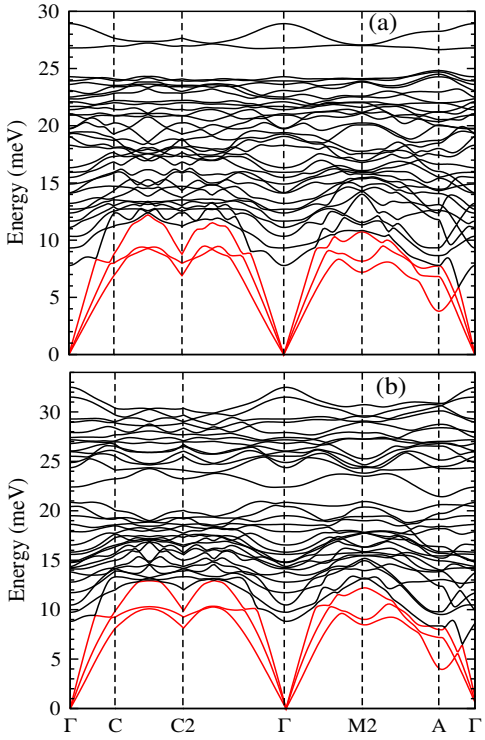

Figure 4: Phonon dispersion of (a) $TaSb_2$ and (b) $NbSb_2$.

3.3. Phonon dispersion

Phonon dispersions of $TaSb_2$ and $NbSb_2$ are presented in Fig. 4 along the high symmetry direction Γ–C–C2–Γ–M2–A–Γ. As the primitive unit cell of compounds contains 12 atoms, the phonon dispersion associates with 36 branches. Out of these branches, 3 are acoustic

(plotted by red lines), and the remaining 33 are optical (plotted by black lines). All the branches give positive energies, signifying the mechanical stability of the compound. Two of the optical branches of $TaSb_2$ having energy higher than 25 meV are well separated from other branches. These two branches are nearly degenerate at M2-point and either side of C2-point around 27 meV. Few optical branches of $NbSb_2$ having energy higher than 21 meV are well separated from other branches. The maximum phonon energies are calculated as ∼29.0 meV and ∼32.5 meV for $TaSb_2$ and $NbSb_2$, respectively.

3.4. Calculated transport properties

In this sub-section, we discuss the calculated transport properties, *viz.,* the temperature dependence of Seebeck coefficient (S), electrical conductivity divided by relaxation time (σ/τ) and electronic thermal conductivity divided by relaxation time (κ_e/τ) as calculated using the BoltzTraP2 package [54] under semi-classical Boltzmann theory. The BoltzTrap2 is based on the combined constant relaxation time approximation (CRTA) and rigid band approximation (RBA). In CRTA, relaxation time (τ) is considered as a constant, but in principle τ is dependent on both band index and wave vector direction. The RBA means that the band-structure is independent of temperature and doping. Considering the CRTA, the σ/τ, S and κ_e/τ can be calculated using the following Boltzmann transport equations (BTE):

$$\sigma/\tau = e^2 \int d\varepsilon \left(-\frac{\partial f_0}{\partial \varepsilon} \right) \sum_{\mathbf{k}} \mathbf{v}_{\mathbf{k}}^2 \delta(\varepsilon - \varepsilon_{\mathbf{k}}), \quad (1)$$

$$S = \frac{e k_B \tau}{\sigma} \int d\varepsilon \left(-\frac{\partial f_0}{\partial \varepsilon} \right) \sum_{\mathbf{k}} \mathbf{v}_{\mathbf{k}}^2 \delta(\varepsilon - \varepsilon_{\mathbf{k}}) \left[\frac{\varepsilon - \mu}{k_B T} \right], \quad (2)$$

$$\frac{\kappa_e}{\tau} = k_B^2 T \int d\varepsilon \left(-\frac{\partial f_0}{\partial \varepsilon} \right) \sum_{\mathbf{k}} \mathbf{v}_{\mathbf{k}}^2 \delta(\varepsilon - \varepsilon_{\mathbf{k}}) \left[\frac{\varepsilon - \mu}{k_B T} \right]^2 - \frac{\sigma}{\tau} S^2 T, \quad (3)$$

where e, k_B, ε, f_0, $\mathbf{k}$, $\mathbf{v}$, μ are the charge carrier, Boltzmann constant, the energy, the Fermi-Dirac distribution function, the wave vector, the group velocity, and the chemical potential, respectively. The f_0 takes care of the temperature dependency of the compound. The marcasite-type $TaSb_2$ and $NbSb_2$ possess anisotropic crystal structures. However, since the samples prepared in this study are polycrystalline without any preferred orientation, the physical property measurements were conducted in only one direction. Thus, when comparing the calculated transport properties with the experimental ones, we averaged the calculated values over all directions. The calculated direction-dependent transport properties are shown in Fig. S6(a) and (b) in Supplemental Material. Addressing anisotropy using high-quality single crystal is possible future work. Additionally, we acknowledge that CRTA simplifies the complex nature of TE transport by assuming a constant relaxation time, which may not fully capture the anisotropic characteristics and off-stoichiometry of the materials. Anisotropic materials often display direction-dependent properties, while stoichiometric deviations can introduce localized states and additional scattering mechanisms that CRTA may not accurately account for. To improve the accuracy of the results, it would be beneficial to consider energy- and direction-dependent scattering rates and potential variations in relaxation time due to off-stoichiometry. While this approach would provide a more detailed understanding of the TE transport, it is also time-consuming and computationally expensive, posing practical challenges.

At first, we discuss the S followed by σ/τ and κ_e/τ. Initially, the S are calculated at E_F (i.e., at μ = 0 eV), which are ∼1 and ∼20 μV K^{-1} at 310 K for $TaSb_2$ and $NbSb_2$, respectively. These positive values of S are far away from the experimental negative values of ∼ −10 and ∼ −21 μV K^{-1} for $TaSb_2$ and $NbSb_2$, respectively at the same temperature. At this point, it is important to note that the calculations of S have been done on single crystalline stoichiometric compounds. But, it is very common to have off-stoichiometry in any synthesized polycrystalline samples. This off-stoichiometry may come from many factors, including the purity of the starting materials, inaccuracy in weighing the raw materials, inhomogeneous mixing during the synthesis process, evaporation of low melting element during the heat treatment etc. These factors are mainly responsible for the defects and/or disorders in the samples which may affect the S of the sample. Here we do not consider any structural imperfections influencing the transport properties, such as changes in oxidation states, anti-site defects, and vacancies, although considering these factors can improve the prediction accuracy. In addition to this, the anisotropy often matters when comparing the calculation of single crystal with the experimental polycrystalline one. All these factors can be addressed in the calculation by shifting the chemical potential (μ) of the compound. But, quantifying the exact value of μ is a challenging job for any compound. For doing this, we have calculated μ dependent S at different temperatures as shown in Fig. 5. Then, the μ has been chosen at 300 K for a better representation of experimental S. We found that at $\mu \approx 64$ and 82 meV, the calculated T dependent S gives the best match with the experimental T dependent S for $TaSb_2$ and $NbSb_2$ as shown in Fig. 6 (a) and (b), respectively. This constant μ calculated

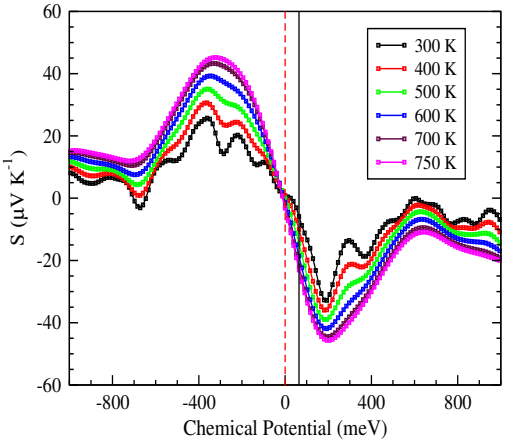

Figure 5: Calculated Seebeck coefficient, S at the function of chemical potential, μ at different temperatures of $TaSb_2$. The solid vertical black line indicates the μ value, where transport properties are calculated.

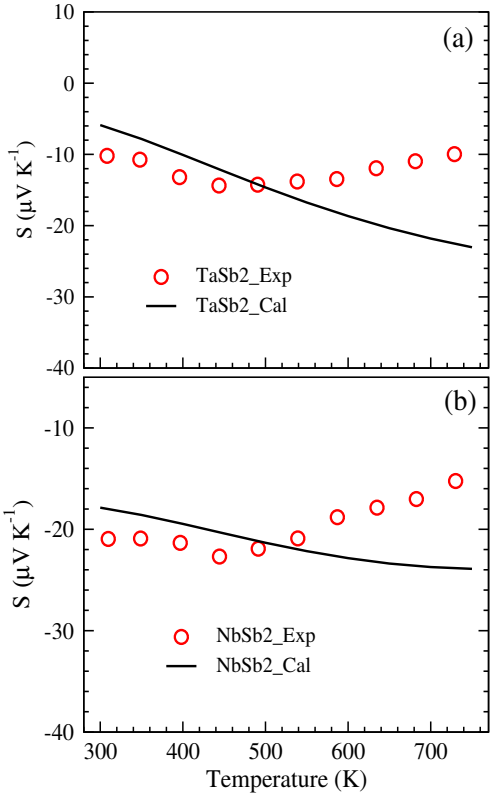

Figure 6: Comparison of experimental and calculated Seebeck coefficients, S of (a) $TaSb_2$ and (b) $NbSb_2$.

at 300 K is used to calculate the other transport properties in the full temperature range.

The T dependent S of $TaSb_2$ and $NbSb_2$ at $\mu \approx 64$ and 82 meV, respectively can be understood through electron/hole pockets formed with the bands 1 and 2 in the band-structure of Fig. 3(a) and (c). The black horizontal dotted lines above the E_F indicate the μ values, where the temperature dependent S are calculated. For both compounds, it is clear that in S, the contributions of charge carriers mainly come from the hole pockets formed with band 1 at the vicinity of Γ and A points and in the Γ–M2 direction, and electron pockets formed with the band 2 in the C–C2, C2–Γ, M2–D2, A–L2, Γ–V2 and Γ–M2 (band 1) directions at $\mu \approx 64$ (82) meV. The presence of dominating electron pockets over hole pockets gives the negative S for both compounds. The low magnitude of S can be understood from the calculated m_e^*/m_h^* ratio of ∼1.2 (near to 1) for $TaSb_2$. The size of the hole pockets at Γ point for $TaSb_2$ (at 64 meV) is larger than the hole pocket at Γ point for $NbSb_2$ (at 82 meV), which supports the less magnitude of the S for $TaSb_2$ as compared to that of $NbSb_2$. Noticeably, the experimental $|S|$ for both compounds increases up to ∼450 K, then decreases till the highest temperature. As the S throughout the temperature range are negative, the dominant contribution comes from the electron pockets. After ∼450 K, the contribution of more hole pockets may result in decreasing of $|S|$. However, the calculated S are deviating from the experimental S in the high temperature region. At this conjuncture, it is important to note that the S is calculated using the ground-state band-structures and constant μ of 300 K. But, the band-structure and μ are the temperature dependent quantities. Hence, considering the temperature dependence of these quantities are expected to improve the accuracy of calculated S at higher temperature, which will be our future work.

Fig. 7 shows the σ/τ of $TaSb_2$ and $NbSb_2$ calculated using Equation 1 as implemented in BoltzTraP2. Equation shows that the calculated σ/τ depends on group velocity of an electron, $\frac{\partial f_0}{\partial \varepsilon}$, and number of available states at a given μ. With an increase in temperature, the number of states always increases. Hence, the increasing nature of σ/τ with temperature (Fig. 7) is directly related to the more number of available states at high temperature. Initially, the charge carriers from band 1 at the vicinity of Γ point and in the Γ–M2 direction, and band 2 in the C–C2, M2–D2, A–L2 and Γ–V2 directions are participated in the transport (Fig 3(a)). As the temperature increases, the more charge carriers from band 1 at the vicinity of A point and in the M2–D2 and Γ–V2 directions; the band 2 in C2–Γ direction are expected to contribute in the σ/τ. At high temperature, more charge carriers from the different electron/hole pockets participate in the conduction, and hence σ/τ increases. The calculated temperature dependent σ/τ is compared with the experimental σ (Fig. 2(b)) to extract the temperature dependent

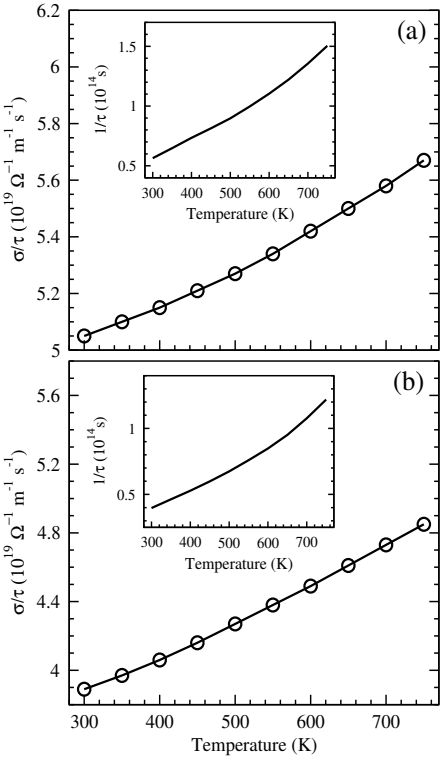

Figure 7: Calculated electrical conductivity divided by relaxation time, σ/τ of (a) $TaSb_2$ and (b) $NbSb_2$. Inset shows $1/\tau$ as a function of temperature, which is estimated by comparing the calculated σ/τ with experimental σ.

$1/\tau$. Insets of Fig. 7 shows the extracted $1/\tau$ in the temperature range of 300–750 K. The values of τ are calculated as $\sim 1.8 \times 10^{-14}$ s and $\sim 2.5 \times 10^{-14}$ s at 300 K for $TaSb_2$ and $NbSb_2$, respectively. With the increase in temperature, $1/\tau$ increases monotonically and reaches the τ values of $\sim 0.66 \times 10^{-14}$ s and $\sim 0.82 \times 10^{-14}$ s at 750 K, respectively. The decreasing nature of τ is due to the presence of more scattering centers at high temperature. For a real system, the calculation of τ is a challenging task due to the involvement of many scattering mechanisms, including electron-electron scattering, electron-phonon scattering, electron-defect scattering etc [8]. This is the reason why we have chosen the simple method to extract temperature dependent τ. This method is previously utilized in literature [67]. It will be interesting to see how this temperature dependent τ explains the other transport properties.

The κ_e/τ for MSb_2 (M = Ta, Nb) are calculated using Equation 3 implemented in BoltzTraP2. As the output of BoltzTraP2 is κ_e/τ, the κ_e is computed using the temperature dependent τ (inset of Fig. 7). Fig. 8 shows the κ_e for $TaSb_2$ and $NbSb_2$ in the temperature region 300–750 K. The calculated κ_e is compared with the experimental κ_e in the same figure. The

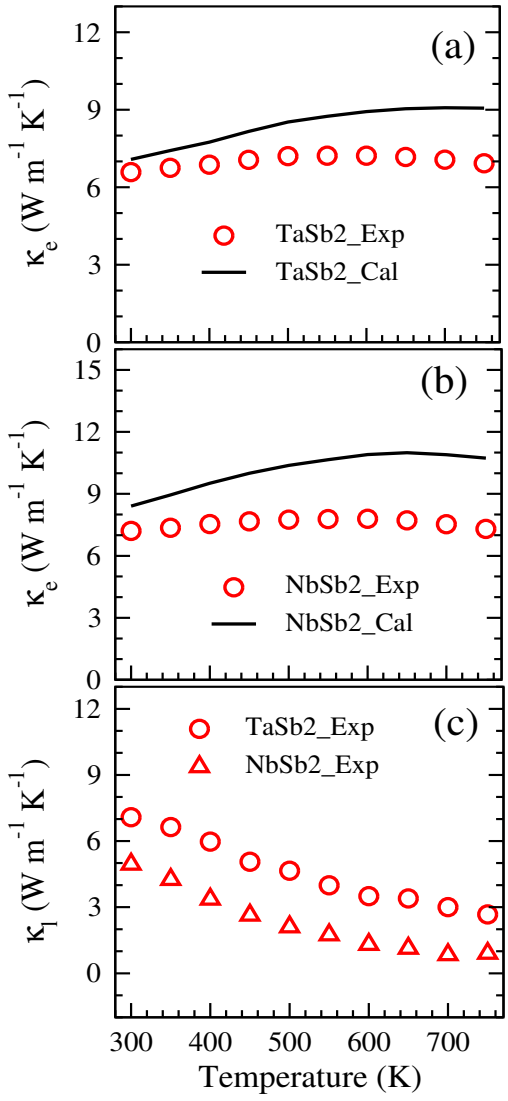

Figure 8: Comparison of experimental (estimated using Wiedemann-Franz law) and calculated electronic part of thermal conductivity, κ_e of (a) $TaSb_2$ and (b) $NbSb_2$. (c) Experimental lattice thermal conductivity calculated using the formula: $\kappa_l = \kappa - \kappa_e$

experimental κ_e is estimated using Wiedemann-Franz law: $\kappa_e = L\sigma T$. Here, the temperature dependent experimental σ (Fig. 2(b)) and the constant value of L ($\sim 2.45 \times 10^{-8}$ W Ω K^{-2}) are taken to estimate the experimental κ_e. However, the L is temperature dependent quantity, and the temperature dependency of L is estimated from the calculated σ/τ and κ_e/τ as shown in Fig. 9. The L at 300 K are found to be $\sim 2.63 \times 10^{-8}$ W Ω K^{-2} and $\sim 2.86 \times 10^{-8}$ W Ω K^{-2} for $TaSb_2$ and $NbSb_2$, respectively. The L increases as the temperature increases. Fig. 8(c) illustrates the experimental κ_l, which is obtained by subtracting the experimental κ_e (estimated using the

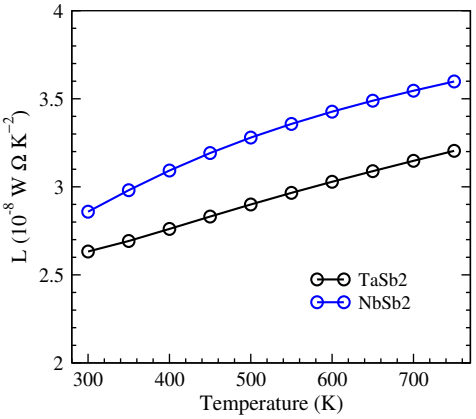

Figure 9: Temperature dependent Lorenz number, L, estimated from the calculated σ/τ and κ_e/τ.

Wiedemann-Franz law) from the total experimental κ. As the temperature rises, there is a notable decrease in κ_l for both compounds. Specifically, at 300 K, the calculated κ_l values are 7.1 and 4.9 W m^{-1} K^{-1}, while these values decrease to 2.7 and 0.9 W m^{-1} K^{-1} at 750 K for $TaSb_2$ and $NbSb_2$, respectively. This trend indicates that at lower temperatures, both electrons and phonons contribute almost equally to the overall κ. However, as the temperature increases, the contribution of phonons to the κ diminishes significantly, making the electronic contribution much more dominant in the heat transfer process. Moreover, from Fig. 8 (a) and (b), it is observed that the calculated κ_e gives quite good agreement with the experimental κ_e. With an increase in temperature, κ_e increases due to contributions of more charge carriers from the different electron/hole pockets. The figure shows that there is a small deviation at high temperature region. At this point, it is important to note that the calculations have been done using ground-state band-structure and constant μ values, as we mentioned earlier. Considering temperature dependency of all these factors may improve the reproducibility at high temperature, which demands extra computational costs.

3.5. Power factor

Finally, the chemical potential dependence of the power factor divided by relaxation time of MSb_2 (M = Ta, Nb) is calculated in the temperature range of 300–1000 K as shown in Fig. 10. The red vertical dashed line at zero eV indicates the Fermi level of the compound. The black vertical solid line at ∼64 and ∼82 meV of $TaSb_2$ and $NbSb_2$, respectively indicates the μ value, at which the transport properties are calculated to explain the experimental results. Using the temperature dependent τ (inset of Fig. 7), the chemical potential dependence of the power factor is calculated in the temperature range of 300–700 K as shown in Fig. 11. The maximum possible power factors are also calculated for p-type and n-type of these compounds. The maximum power factors for p-type conduction are calculated as ∼1.14 and ∼1.74 mW m^{-1} K^{-2} at ∼ −375 and ∼ −320 meV, respectively at 300 K. These values are found to be ∼1.16 and ∼1.80 mW m^{-1} K^{-2} at ∼215 and ∼215 meV for n-type of $TaSb_2$ and $NbSb_2$, respectively at 300 K. The p-type and n-type are confirmed from the sign of S at the corresponding μ values of Fig. 5. The τ values are taken from the previous calculations (Inset of Fig. 7). The carrier concentrations corresponding to the maximum power factors for p-type of $TaSb_2$ and $NbSb_2$ are calculated as ∼2.56 × 10^{21} and ∼2.60 × 10^{21} cm^{-3}, respectively, whereas for the n-type conduction of $TaSb_2$ and $NbSb_2$ these values are found to be ∼1.42 × 10^{21} and ∼1.58 × 10^{21} cm^{-3}, respectively. The predicted power factors at 300 K in this study are comparable with the power factors of ∼1–2 mW m^{-1} K^{-2} for Bi_2Te_3 parent compound [68–70], though the power factors of BiTe-based doped compounds are reported as ∼4–7 mW m^{-1} K^{-2} in many literatures [71–74] at/around the room temperature. However, the power factor of many semimetals is reported insensitive to doping concentration [75]. In contrast, the enhancement of the power factor of rare-earth doped semimetal HfTe5 is reported by Lowhorn *et al* [76]. The improvement of the power factors of some semimetallic Heusler alloys are reported by tuning the doping concentration [77, 78]. Moreover, a rigorous effort is required to synthesize the suitable p and n-type doping of MSb_2 (M = Ta, Nb) to validate the computational prediction.

4. Conclusions

The thermoelectric properties of MSb_2 (M = Ta, Nb) are studied in the present study. These compounds were prepared by a combined solid-state reaction and a spark plasma sintering process. The monoclinic phase with space group $C2/m$ is confirmed for both compounds through Rietveld refinement. The negative sign of the Seebeck coefficient indicates the n-type behaviour of these compounds. The DFT-based electronic structure calculations were carried out in order to understand the experimentally observed thermoelectric properties. The semimetallic behaviour of these compounds was confirmed from the band-structure and density of states calculations. The multi-band electron and hole pockets are found reasonably good in explaining the experimental results. Further study of computational calculations gives the maximum possible power factors of ∼1.14 and ∼1.74

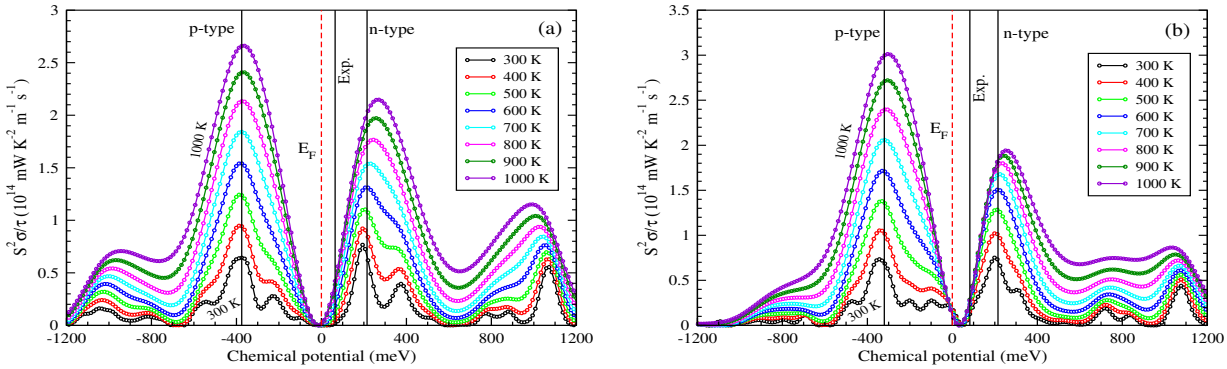

Figure 10: Variation of power factor ($S^2\sigma$) per relaxation time with chemical potential at different temperatures of (a) $TaSb_2$ and (b) $NbSb_2$.

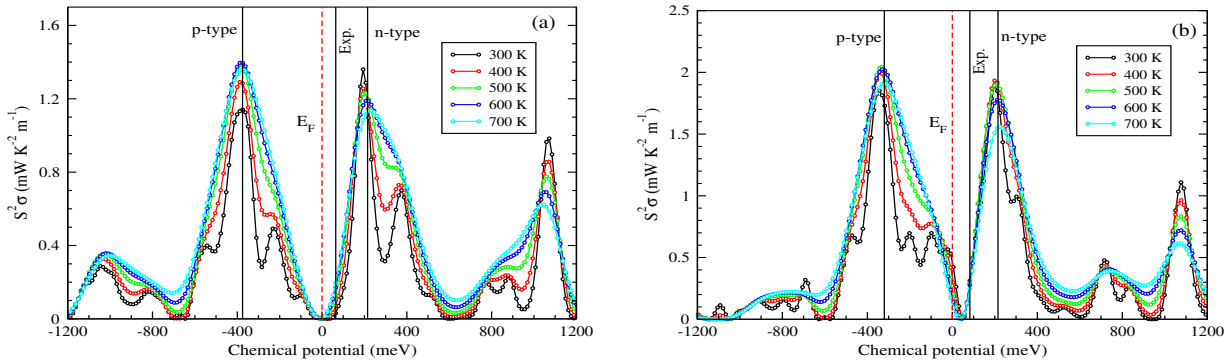

Figure 11: Variation of power factor ($S^2\sigma$) with chemical potential at different temperatures of (a) $TaSb_2$ and (b) $NbSb_2$.

mW m^{-1} K^{-2} for p-type conduction of $TaSb_2$ and $NbSb_2$, respectively at 300 K, while these values are found to be ∼1.16 and ∼1.80 mW m^{-1} K^{-2} at 300 K for n-type conduction, respectively with the corresponding concentrations. According to the calculations, a relatively high power factor can be achieved, but since the required carrier concentration is high, it should be noted that the rigid band approximation is properly maintained. In conclusion, the combined DFT and Boltzmann transport theory are found to be reasonably good at addressing the experimental transport properties, and moderate power factors can be obtained if these compounds are synthesized with the proper doping concentration.

Supplemental material

See the Supplemental Material (SM) for the electronic structure and transport calculations using spin-orbit coupling (SOC).

Data availability statement

The data that support the findings of this study are available within the article and supplementary material.

Acknowledgments

This work was supported by JST Mirai Program Grant Number JPMJMI19A1.

References

[1] G. J. Snyder and E. S. Toberer, Nat. Mater. **7,** 105 (2008).
[2] J. R. Sootsman, D. Y. Chung and M. G. Kanatzidis, Angew. Chem. Int. Ed. **48,** 8616 (2009).
[3] D. Zhao and G. Tan, Appl. Therm. Eng **66,** 15 (2014).
[4] T. Mori, Small **13,** 1702013 (2017).
[5] S. Shittu, G. Li, X. Zhao and X. Ma, Appl. Energy **268,** 115075 (2020).
[6] T. Hendricks, T. Caillat and Takao Mori, Energies **15,** 7307 (2022).
[7] M. d'Angelo, C. Galassi and N. Lecis, Energies **16,** 6409 (2023).
[8] N. W. Ashcroft and N. D. Mermin, Solid State Physics, edited by D. G. Crane, (Saunders College Publishing, New York, 1976), Vol. 239.
[9] S. Sk, P. Devi, S. Singh and S. K. Pandey, Mater. Res. Express **6,** 026302 (2018).
[10] W. M. Yim and F. D. Rosi, Solid State Electron. **15,** 1121 (1972).
[11] O. Yamashita, S. Tomiyoshi and K. Makita, J. Appl. Phys. **93,** 368 (2003).
[12] D. K. Ko, Y. Kang and C. B. Murray, Nano Lett. **11,** 2841 (2011).
[13] K. Biswas, J. Q. He, I. D. Blum, C. I. Wu, T. P. Hogan, D.

N. Seidman, V. P. Dravid and M. G. Kanatzidis, Nature **489,** 414 (2012).
[14] Y. Xiao and L. D. Zhao, npj Quantum Mater. **3,** 55 (2018).
[15] M. Hong, Y. Wang, S. Xu, X. Shi, L. Chen, J. Zou and Z. G. Chen, Nano Energy **60,** 1 (2019).
[16] G. Joshi *et al.*, Nano Lett. **8,** 4670 (2008).
[17] R. Basu and A. Singh, Mater. Today Phys. **21,** 100468 (2021).
[18] H. Tamaki, H. K. Sato and T. Kanno, Adv. Mater. **28,** 10182 (2016).
[19] Z. Liu *et al.*, Joule **5,** 1196 (2021).
[20] Z. Liu, W. Gao, H. Oshima, K. Nagase, C. H. Lee, and T. Mori, Nat. Commun. **13,** 1120 (2022).
[21] L. Wang *et al.*, Adv. Energy Mater. **13,** 2370143 (2023).
[22] N. Wang, H. Chen, H. He, W. Norimatsu, M. Kusunoki and K. Koumoto, Sci. Rep. **3,** 3 (2013).
[23] X. Shi, A. Wu, W. Liu, R. Moshwan, Y. Wang, Z. G. Chen and J. Zou, ACS Nano **12,** 11417 (2018).
[24] A. U. Khan *et al.*, Nano Energy **31,** 152 (2017)
[25] G. Mahan and J. Sofo, Proc. Nat. Acad. Sci. **93,** 7436 (1996).
[26] F. Ahmed, N. Tsujii and T. Mori, J. mater. Chem. A **5,** 7545 (2017).
[27] Z. Liu, W. Gao, W. Zhang, N. Sato, Q. Guo and T. Mori, Adv. Energy Mater. **10,** 2002588 (2020).
[28] C. Bourges, N. Sato, T. Baba, T. Baba, I. Ohkubo, N. Tsujii and T. Mori RSC Advances. **10,** 21129 (2020).
[29] F. Garmroudi *et al.*, Mater. Today Phys. **27,** 100742 (2022).
[30] W. Zhang, J. -F. Halet and T. Mori, Npj Comput. Mater. **9,** 137 (2023).
[31] A. Bentien, S. Johnsen, G. K. M. Madsen, B. B. Iversen and F. Steglich, EPL **80,** 17008 (2007).
[32] P. Sun, N. Oeschler, S. Johnsen, B. B. Iversen and F. Steglich, Dalton Trans **39,** 1012 (2010).
[33] Z. Bai, Y. Ji and B. Qin, J Mater Sci: Mater Electron **34,** 461 (2023).
[34] V. K. Gudelli, V. Kanchana, G. Vaitheeswaran, M. C. Valsakumar and S. D. Mahanti, RSC Adv. **4,** 9424 (2014).
[35] V. K. Gudelli, V. Kanchana, S. Appalakondaiah, G. Vaitheeswaran and M. C. Valsakumar, J. Phys. Chem. C **117,** 21120 (2013).
[36] P. Sun, N. Oeschler, S. Johnsen, B. B. Iversen and F. Steglich, Appl. Phys. Express **2,** 091102 (2009).
[37] P. Sun, N. Oeschler, S. Johnsen, B. B. Iversen, and F. Steglich, J. Phys. Conf. Ser **150,** 012049 (2009).
[38] Y. Li, L. Li, J. Wang, T. Wang, X. Xu, C. Xi, C. Cao and J. Dai, Phys. Rev. B **94,** 121115 (2016).
[39] A. Pariari, R. Singha, S. Roy, B. Satpati and P. Mandal, Sci. Rep. **8,** 10527 (2018).
[40] P. Kumar, Sudesh and S. Patnaik, J. Phys. Commun. **3,** 115007 (2019).
[41] P. Li, P. Qiu, Q. Xu, J. Luo, Y. Xiong, J. Xiao, N. Aryal, Q. Li, L. Chen and X. Shi, Nat. Commun. **13,** 7612 (2022).
[42] P. Li, P. Qiu,J. Xiao, T. Deng, L. Chen and X. Shi, Energy Environ. Sci. **16,** 3753 (2023).
[43] I. Masuda, H. Miyazaki, M. Yoshimura, H. Ishii and Y. Nishino, Phys. Status Solidi B **259,** 2100571 (2022).
[44] F. Failamani *et al.*, Intermetallics **65,** 94 (2015).
[45] K. F. Wang, D. Graf, L. J. Li, and L. M. Wang, Petrovic, C. Sci. Rep. **4,** 7328 (2015).
[46] C. Xu, J. Chen, G. -X. Zhi, Y. Li, J. Dai and C. Cao, Phys. Rev. B **93,** 195106 (2016).
[47] X. Y. Liu *et al.,* Chin. Phys. Lett. **34,** 127501 (2017).
[48] D. Gresch, Q. S. Wu, G. W. Winkler and A. A. Soluyanov, New J. Phys. **19,** 035001 (2017).
[49] L. Guo *et al.,* J. Appl. Phys. **123,** 155103 (2018).
[50] C. Gayner and Y. Amouyal, Adv. Funct. Mater. **30(18),** 1901789 (2020).
[51] W. Kohn and L. J. Sham, Phys. Rev. **140**, A1133 (1965).
[52] P. Giannozzi *et al.*, J. Phys. Condens. Matter **21,** 395502 (2009).
[53] J. P. Perdew and A. Zunger, Phys. Rev. B **23,** 5048 (1981).
[54] G. K. H. Madsen, J. Carrete and M. J. Verstraete, Comput. Phys. Commun. **231**, 140 (2018).
[55] A. F. Ioffe, Physics of Semiconductors (Infosearch Limited, London, 1960).
[56] G. Li *et al.*, Chem. Mater. **27**, 8220 (2015).
[57] K. Kaur, S. Dhimanb and R. Kumar, Physics Letters A, **381(4),** 339 (2017).
[58] B. Skinner and L. Fu, Science Advances, **4,** 2621 (2018).
[59] Y. Pan *et al.*, Adv. Mater., **33(7),** 2003168 (2021).
[60] M. Markov, X. Hu, H. C. Liu, N. Liu, S. J. Poon, K. Esfarjani, and M. Zebarjadi, Sci. Rep. **8(1),** 9876 (2018).
[61] J. Mao, H. Zhu, Z. Ding, Z. Liu, G. A. Gamage, G. Chen and Z. Ren, Science **365** 498 (2019).
[62] M. Markov *et al.,* Phys. Rev. Materials **3,** 095401 (2019).
[63] S. E. Lee M. J. Oh, S. Ji, J. Kim, J. H. Jun, W. Kang, Younjung Jo and M. H. Jung Proc. Natl Acad. Sci. USA **118,** e2023027118 (2021).
[64] The Materials Project, Materials Data on $TaSb_2$ by Materials Project, United States, 2015, doi:10.17188/1188289.
[65] Data retrieved from the Materials Project for $NbSb_2$ (mp-1969) from database version v2023.11.1.
[66] Y. Zhou *et al.,* J. Solid State Chem. **265,** 359 (2018).
[67] S. Sk, N. Shahi and S. K. Pandey, J. Phys.: Condens. Matter **34,** 265901 (2022).
[68] J. F. Li and J. Liu, Phys. Stat. Sol. (a) **203,** 3768 (2006).
[69] L. D. Zhao, B. P. Zhang, W. S. Liu and J. F. Li, J. Appl. Phys. **105,** 023704 (2009).
[70] J. Fu, S. Song, X. Zhang, F. Cao, L. Zhou, X. Li and H. Zhang, Crys. Eng. Comm **14,** 2159 (2012).
[71] O. Yamashita, S. Tomiyoshi and K. Makita, J. Appl. Phys. **93,** 368 (2003).
[72] O. Yamashita and S. Tomiyoshi, J. Appl. Phys. **95,** 6277 (2004).
[73] B. Poudel *et al.*, Science **320,** 634 (2008).
[74] K. Park *et al.*, J. Am. Chem. Soc. **138,** 14458 (2016).
[75] M. Markov, S. E. Rezaei, S. N. Sadeghi, K. Esfarjani and M. Zebarjadi, Phys. Rev. Materials **3,** 095401 (2019).
[76] N. D. Lowhorn, T. M. Tritt, E. E. Abbott and J. W. Kolis, Appl. Phys. Lett. **88,** 022101 (2006).
[77] F. Garmroudi *et al.,* Materials Today Physics **27,** 100742 (2022).
[78] Y. Xia, S. Bhattacharya, A. L. Pope, S. J. Poon and T. M. Tritt, J. Appl. Phys. **88,** 1953 (2000).